

Considerations for extracting moiré-level strain from dark field intensities in transmission electron microscopy

Isaac M. Craig,¹ Madeline Van Winkle,¹ Colin Ophus,² and D. Kwabena Bediako^{1,3}

¹*Department of Chemistry, University of California, Berkeley*

²*The Molecular Foundry, Lawrence Berkeley National Laboratory, Berkeley*

³*Chemical Sciences Division, Lawrence Berkeley National Laboratory*

(*bediako@berkeley.edu)

(Dated: 10 June 2024)

Bragg interferometry (BI) is an imaging technique based on four-dimensional scanning electron microscopy (4D-STEM) wherein the intensities of select overlapping Bragg disks are fit or more qualitatively analyzed in the context of simple trigonometric equations to determine local stacking order. In 4D-STEM based approaches, the collection of full diffraction patterns at each real-space position of the scanning probe allows the use of precise virtual apertures much smaller and more variable in shape than those used in conventional dark field imaging, such that even buried interfaces marginally twisted from other layers can be targeted. A coarse-grained form of dark field ptychography, BI uses simple physically derived fitting functions to extract the average structure within the illumination region and is therefore viable over large fields of view. BI has shown a particular advantage for selectively investigating the interlayer stacking and associated moiré reconstruction of bilayer interfaces within complex multi-layered structures. This has enabled investigation of reconstruction and substrate effects in bilayers through encapsulating hexagonal boron nitride and of select bilayer interfaces within trilayer stacks. However, the technique can be improved to provide a greater spatial resolution and probe a wider range of twisted structures, for which current limitations on acquisition parameters can lead to large illumination regions and the computationally involved post-processing can fail. Here we analyze these limitations and the computational processing in greater depth, presenting a few methods for improvement over previous works, discussing potential areas for further expansion, and illustrating the current capabilities of this approach for extracting moiré-scale strain.

I. INTRODUCTION

Moiré materials, formed by stacking atomically thin materials with a slight interlayer twist or lattice mismatch, exhibit spatially modulated potentials that can localize excitons and charge carriers, serving as a basis for many novel devices.^{1–11} Both highly tunable and proposed to be a physical realization of the Hubbard model with experimentally accessible transition temperatures, moiré materials are also a preferred platform to investigate correlated effects.^{1,2,12–20} However as these materials locally reconstruct^{21–26} in a manner that alters their electronic behavior^{27–32}, a detailed understanding of the reconstruction mechanism in these systems is crucial to realize practical devices and further our understanding of their rich physics.

We discuss an interferometric methodology based on four-dimensional scanning transmission electron microscopy^{33–35} that permits the direct measurement of inter-layer strain fields.^{24,36} This approach involves fitting interference fringes in the diffraction patterns to a known functional form to extract structural details.^{24,36,37} Alternative 4D-STEM based methods typically fit the locations of Bragg disks^{38–42}, or have analyzed a combination of both intensity and disk locations⁴³. However, determining the locations of these large converged beam electron diffraction (CBED) disks to the precision needed for revolving moiré-level strain is difficult without specialized apertures⁴⁴ and has not yet been feasible in marginally twisted structures. Other ptychographic techniques similarly analyze scattering intensities and can provide much higher resolution^{45–48}, but are currently arduous to acquire and analyze over the moiré length scale. BI avoids the

same level of computational complexity by only fitting select areas in the acquired diffraction patterns of anticipated interest for determining moiré stacking to simple physically derived analytical expressions, omitting the central beam and averaging over the sample within the illuminated region to provide a coarse-grained picture of reconstruction on the moiré-scale.

We outline how this interferometric methodology can measure strain from bilayer interfaces in generic structures and discuss and present solutions to various numerical challenges encountered in its practical application. Numerical approaches for the fitting and extraction of strain are compared, and various considerations are presented for improved strain resolution and analyzed using simulated multi-slice data and through re-processing published^{24,36} data.

II. STRAIN FIELDS IN MOIRÉ SYSTEMS

We begin with a simple picture of strain in moiré materials. We can first assume that there is negligible hetero-strain within the moiré such that the lattice vectors of both layers are identical apart from a small interlayer twist angle θ , (Figure 1a), resulting in the following relationship between the atomic positions of the top layer $\mathbf{r}_{ij}^{\text{top}}$, the bottom layer $\mathbf{r}_{ij}^{\text{bottom}}$, and the reference layer $\mathbf{r}_{ij}^{\text{ref}}$ we take as halfway between them at each pixel location (i, j) . The details of the \mathbf{r}_{ij} coordinates do not factor into this analysis as we consider the strain of the locally averaged offset between the lattice vectors of each layer.

$$\mathbf{r}_{ij}^{\text{top}} = \begin{bmatrix} \cos(\frac{\theta_t}{2}) & -\sin(\frac{\theta_t}{2}) \\ \sin(\frac{\theta_t}{2}) & \cos(\frac{\theta_t}{2}) \end{bmatrix} \mathbf{r}_{ij}^{\text{ref}}$$

$$\mathbf{r}_{ij}^{\text{bottom}} = \begin{bmatrix} \cos(\frac{\theta_t}{2}) & \sin(\frac{\theta_t}{2}) \\ -\sin(\frac{\theta_t}{2}) & \cos(\frac{\theta_t}{2}) \end{bmatrix} \mathbf{r}_{ij}^{\text{ref}}$$

The expression is straightforwardly adapted to account for an interlayer lattice mismatch originating either in hetero-strain or from the use of two chemically distinct layers. The intralayer displacement \mathbf{u}^{top} (Fig 1b) associated with the displacement of each atom in the top layer away from the reference is therefore given by $\mathbf{u}_{ij}^{\text{top}} = (\mathbf{r}_{ij}^{\text{top}} - \mathbf{r}_{ij}^{\text{ref}})$, yielding the following relation.

$$\mathbf{u}_{ij}^{\text{top}} = \begin{bmatrix} \cos(\frac{\theta_t}{2}) - 1 & -\sin(\frac{\theta_t}{2}) \\ \sin(\frac{\theta_t}{2}) & \cos(\frac{\theta_t}{2}) - 1 \end{bmatrix} \mathbf{r}_{ij}^{\text{ref}}$$

Likewise, we define $\mathbf{u}_{ij}^{\text{bottom}} = (\mathbf{r}_{ij}^{\text{bottom}} - \mathbf{r}_{ij}^{\text{ref}})$. These displacements can be analyzed using small displacement theory (also known as infinitesimal strain theory)⁴⁹, in which the strain tensors are linearized. This framework neglects higher-order terms from changes to the coordinate system, omitting the distinction between deformed and reference axes. Such an approximation is valid when the displacements change relatively slowly over the field of view such that $|\nabla \mathbf{u}^{\text{top}}|_{\infty} \ll 1$. This necessitates that the relaxation is not too dramatic and that the lattice scale a_0 is much smaller than the moiré-wavelength, coinciding with a small interlayer twist. More precisely, the local deformation gradient within a rigid structure is on the order of $\sin(\theta/2)$ as $\mathbf{u}_{ij}^{\text{top}}$ varies between 0 and $a_0/4$ over a length scale $a_0/\sin(\theta/2)$. The following analysis therefore assumes $\sin(\theta/2) \ll 1$.

The strain tensor $\nabla \mathbf{u}_{ij}^{\text{top}}$ then consists of partial derivatives of $\mathbf{u}_{ij}^{\text{top}}$ with respect to the reference coordinates. For a rigidly twisted structure that perfectly obeys this relation at each pixel, $\nabla \mathbf{u}_{ij}^{\text{top}}$ is independent of pixel location and obeys the following uniformly.

$$\nabla \mathbf{u}_{ij}^{\text{top}} = \begin{bmatrix} \cos(\frac{\theta_t}{2}) - 1 & -\sin(\frac{\theta_t}{2}) \\ \sin(\frac{\theta_t}{2}) & \cos(\frac{\theta_t}{2}) - 1 \end{bmatrix} \quad (1)$$

This rigid displacement field corresponds to a uniform local curl and divergence of $\nabla \times \mathbf{u}_{ij}^{\text{top}} = 2\sin(\theta_t/2)$ and $\nabla \cdot \mathbf{u}_{ij}^{\text{top}} = 2\cos(\theta_t/2) - 2$, equal to θ_t and 0 respectively to first order. Atomic reconstruction will manifest deviations from this uniform curl and divergence, which we will denote as rotations and dilations respectively. The use of small deformation theory further permits us to consider reconstruction-driven changes to the local rotation and dilation as additive changes to what is expected of a rigid moiré. In this framework, we can decompose $\nabla \mathbf{u}^{\text{top}}$ as the sum of the curl-free and divergence-free matrices ε and ω , encoding dilational and rotational strain respectively.

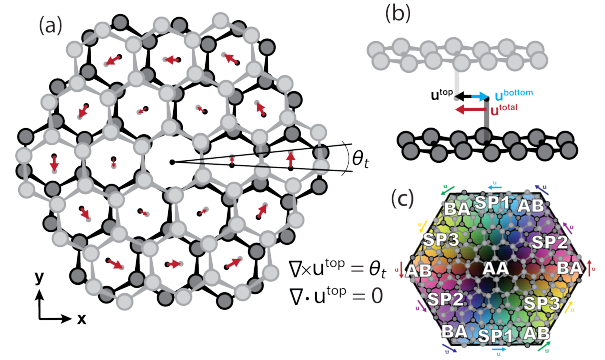


FIG. 1. **(1a)** Schematic illustrating the anticipated interlayer displacements $\mathbf{u}^{\text{total}}$ within a rigid moiré structure at a twist angle of θ_t , for which the curl and divergence of the displacement \mathbf{u}^{top} (equal to one half $\mathbf{u}^{\text{total}}$) are uniformly θ_t and 0 respectively. **(1b)** Definition of the total interlayer displacement $\mathbf{u}^{\text{total}}$, where $\mathbf{u}^{\text{total}} = \mathbf{u}^{\text{top}} + \mathbf{u}^{\text{bottom}}$ in terms of the intralayer displacements of each layer, \mathbf{u}^{top} and $\mathbf{u}^{\text{bottom}}$. $|\mathbf{u}^{\text{top}}| \approx |\mathbf{u}^{\text{bottom}}|$ such that $\mathbf{u}^{\text{total}} \approx 2\mathbf{u}^{\text{top}}$ is assumed. **(1c)** Legend illustrating the coloring scheme used to denote the atomic stacking, where AA denotes regions where the two layers are aligned out-of-plane and AB/BA denote regions where the two layers are aligned Bernal out-of-plane. SP1, SP2, and SP3 denote the various symmetrically distinct saddle point stacking regions.

$$\nabla \mathbf{u}^{\text{top}} = \underbrace{\frac{1}{2} \nabla \mathbf{u}^{\text{top}} + \frac{1}{2} (\nabla \mathbf{u}^{\text{top}})^T}_{\varepsilon} + \underbrace{\frac{1}{2} \nabla \mathbf{u}^{\text{top}} - \frac{1}{2} (\nabla \mathbf{u}^{\text{top}})^T}_{\omega}$$

The eigenvalues and eigenvectors of ε are termed the principal stretches and their directions, and the sum and difference of these eigenvalues are the total intralayer dilation (the first invariant, equivalent to $\nabla \cdot \mathbf{u}^{\text{top}}$) and maximum intralayer engineering shear strain γ respectively. The curl of ω corresponds to the local rotation $\nabla \times \mathbf{u}^{\text{top}}$, consisting of the sum of the rigidly imposed twist angle and a local reconstruction rotation. For a homo-bilayer structure, the deformation of the top and bottom layers are equal and opposite and all reconstruction information can be determined through consideration of a single layer. In the discussion that follows, we use \mathbf{u} to denote $\mathbf{u}^{\text{total}}$.

III. INTERFERENCE REGION INTENSITIES FOR DISPLACEMENT MEASUREMENTS

To extract these displacements \mathbf{u} and associated strain $\nabla \mathbf{u}$, we look at the intensity of the overlap regions between Bragg disks arising from the scattering off of desired layers in the material. The overlap intensities I_j at reciprocal lattice positions \mathbf{g}_j can be shown to obey the following equation, where \mathbf{u} is the (in-plane projection of the) interlayer displacement vector dictating stacking order.

$$I_j = A_j + B_j \cos^2(\pi \mathbf{g}_j \cdot \mathbf{u}) \quad (2)$$

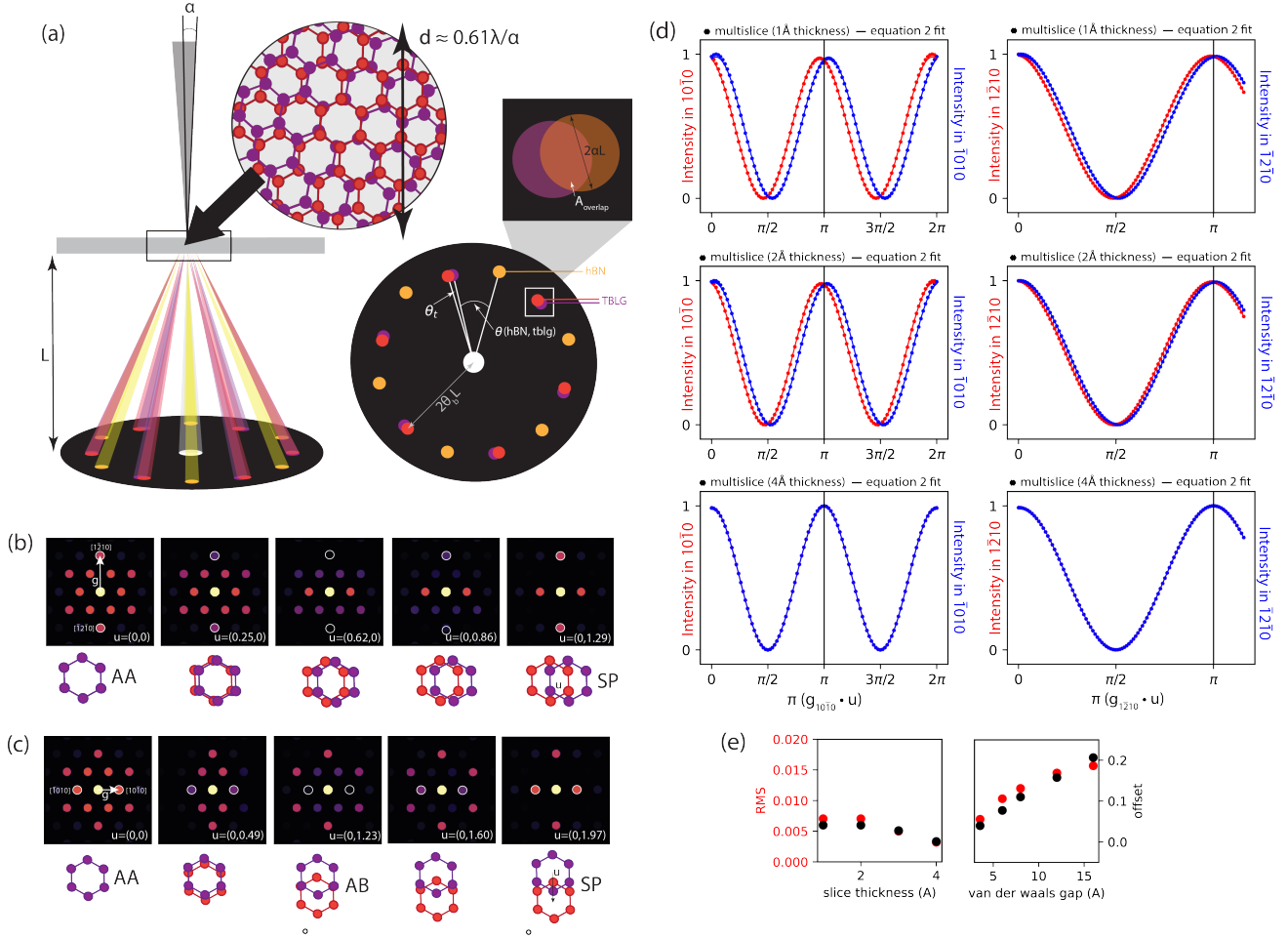


FIG. 2. **(2a)** Schematics illustrating the 4D-STEM Bragg interferometry approach where a series of converged beam electron diffraction patterns are collected at various real-space positions as the beam is scanned across the sample. Various relevant parameters including the camera length L , convergence semi-angle α , and electron probe width d are noted. **(2b-c)** Multi-slice CBED patterns at select u choices. Corresponding approximate real space stackings are below. $10\bar{1}0$ and $\bar{1}210$ reflections are highlighted in white, corresponding to those plotted in 2d. **(2d)** Variation in intensity of the $10\bar{1}0$ and $\bar{1}210$ reflections (red) and their Friedel pairs (blue) over a densely-sampled scan of u choices. These reflections were selected for ease as they align with the chosen cartesian axis orientation. Both intensities show good agreement with a fit to equation 2 (solid lines) with the need for a small offset from the origin, equal and opposite for each Friedel pair. **(2e)** Corresponding root mean squared errors and offsets added to the cosine argument are shown for the $10\bar{1}0$ line-cut (left column of 2d) in units of π for a series of acquisition parameters. Unless otherwise noted, multi-slice simulations were carried out using $\alpha = 4$ mrad, a slice thickness of 3 Å, perfect aberration correction, and the VdW gap expected for graphene of 3.55Å using AbTEM⁵⁰

The full derivation is shown in the supplemental information of²⁴ and³⁶ for a centro-symmetric homo-bilayer and a general bilayer respectively. Briefly, a series of strict assumptions (that the beam is completely focused and that scattering takes place within a single plane and is well represented by the weak phase object approximation) are used to yield the simple analytic expression above.

The accuracy of this expression can be investigated through comparison to simulated electron diffraction patterns, obtained using the multi-slice algorithm.⁵¹ In figure 2, we present multi-slice results obtained at a series of van-der waals (VdW) gap choices and multi-slice thicknesses, parameterizing the number of scattering events. Each multi-slice simula-

tion is performed on a large uniform bilayer graphene sheet of a given stacking order to investigate the accuracy of equation (2) without resolution considerations, which will be discussed in a later section. An α of 4 mrad and a perfectly focused aberration-free lens are assumed. We note that the primary effect of changing α in the absence of resolution considerations will be to increase the impact of small aberrations not included here. Aberrations will also change the internal structure of the overlap intensity, effects from which can be mitigated through averaging over the whole overlap region. The implications of subtle internal structure in aberrated probes for non-spherical virtual apertures is outside the scope of this paper. The defocus also will have little impact when resolution considera-

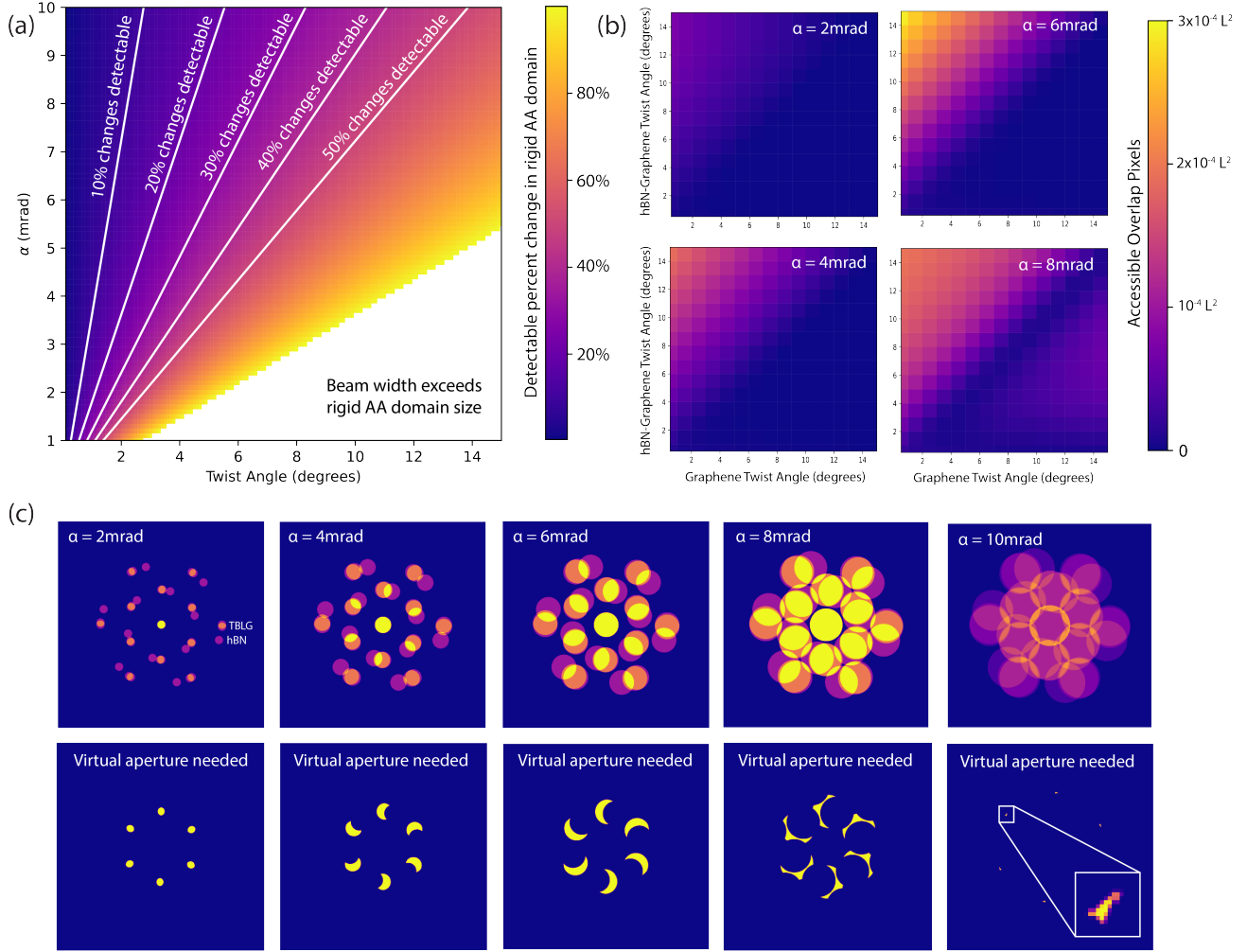


FIG. 3. **(3a)** Convergence semi-angle α needed to resolve AA-type domain contractions to a given precision. The probe size is assumed to be $0.61 \lambda / \alpha$, AA region defined as $|u| = 0 \pm 0.25a_0$, and domain size changes are taken to be observable when larger than the beam width. The α needed will be over-estimated as observed beam widths are slightly smaller than those predicted and many independent measurements are used. **(3b)** To-scale illustrations of the overlap regions expected at a series of α choices for a hBN, bilayer graphene hetero-structure with inter-layer twists of 2 degrees, 15 degrees, and 17 degrees between the two graphene layers and each graphene layer and the hBN respectively. **(3c)** Number of viable overlap pixels in units of the camera length squared for a series of twist angles and α choices. The two smallest of the three twist tables are labeled, with the third implicit angle being the sum of these other two.

tions are ignored so long as the entire overlap region intensity is averaged³⁷.

Fig. 2d shows a slight disagreement between Eqn 2. and the multi-slice results. This discrepancy presents as a slight decrease in the multi-slice intensity of the second-order reflections in the AA-type stacking region and a small offset of the cosine origin. Increasing the VdW gap of the material leads to a greater deviation from the expected expression, as it is derived under the assumption that the free-space propagation present in multi-slice between the two layers plays a minor role. However, the expression remains accurate up to at least gaps of 15 angstroms. We note that these discrepancies are far too small to be seen in the experimental data due to the effects of noise and finite resolution for materials with

relatively small VdW gaps, but may need to be considered in bilayer materials with many intermediate layers between.

The slight discrepancy between equation (2) and the multi-slice results obtained using a slice thickness greater than the VdW gap (and therefore a single scattering event) can be attributed to the weak phase object assumption. The goodness of fit for the data simulated with a 4\AA slice thickness reflects that the weak phase object assumption is well motivated for bilayer graphene and slight deviations from equation (2) are primarily driven by multiple scattering. We conclude that the presented expression is sufficient for describing the intensity variations in graphene bilayers and inaccuracies arising from finite spatial resolution, post-processing, and experimental considerations such as sample purity will dominate.

IV. RESOLUTION-DRIVEN RESTRICTIONS ON SAMPLE MORPHOLOGY

One major resolution limiting consideration in previous studies was the effect of beam-width biasing, as previous works reported stacking order and strain averaged over illumination regions of approximately 1 to 1.5 nm. These probe sizes are also larger than those seen in other electron microscopy techniques⁴⁵⁻⁴⁸, which often use probe widths on the order of 0.2-0.5 nm and also analyze the sample variability within illumination regions to obtain sub-angstrom resolution. Unlike many microscopy techniques, the minimum viable spatial resolution of BI is dependent on the sample morphology. To understand why we first note that the full-width at half maximum of the point spread function, or the modulo square of Fourier transform of $\exp(i\chi)$ where χ is the Scherzer aberration function⁵², and α -dependent phase shift introduced by the lens, yields a typical measure for probe width.⁵³ For many applications, the maximum tolerable phase error is then used to determine the maximal semi-convergence angle (α) and its associated probe width of approximately $0.61 \lambda/\alpha$ where λ is the wavelength of the electron probe (Figure 1e).⁵⁴ We will not consider the effect of this phase error on the CBED pattern signal to noise as it is beyond the scope of this work, instead focusing on $\alpha < 10$ mrad where it is deemed tolerable with sufficient aberration correction⁵⁴ and consider the number of pixels we can obtain at each α and the practical limitations associated with their extraction.

In BI, we often cannot realize the optimal α as the large convergence angle will lead to an overlap of additional Bragg disks and prohibit the selective investigation of desired interfaces. To see how these considerations translate to the obtained spatial resolution, we first note that the probe wavelength we use is associated with a relatively low 80 kV accelerating voltage, which increases the probe width. The use of lower accelerating voltages is however more necessary in thin samples to reduce knock-on damage⁵⁵⁻⁵⁷. The resulting probe width provides us with a measure of our spatial resolution, where we can assess changes in average displacement down to a minimum spatial resolution of roughly d if not slightly smaller⁵⁸. This can be used to determine the minimum α needed at each twist angle to resolve stacking order domain size changes to a given precision. For this, we define the AA stacking domains to include stacking configurations of $|\mathbf{u}| = 0 \pm 0.25a_0$ so that a rigidly twisted structure has AA domains of width $0.25a_0/\sin(\theta/2)$. The α needed to resolve domain contractions to a given percent of the rigid value are shown in Figure 3a. We note that the BI methodology is most suitable for relatively small twist angles where dramatic changes to the AA domains are seen.

For many sample morphologies, α must be smaller than 10 mrad. To see this, we show a series of anticipated overlap regions (Figure 3b), obtained using the relations illustrated in Figure 1a-b. We can then straightforwardly compute the number of overlap pixels (in units of the camera length squared) at a given choice of sample morphology and α . We also note that small overlap regions are difficult to isolate in practice. This currently limits the spatial resolution and the range of samples

that can be investigated with this technique. However larger α and therefore higher spatial resolution are possible than those used in previous works ($\alpha \approx 2 - 3$ mrad)^{24,36} if care is taken to define precise virtual apertures of variable shape (Figure 3c) instead of avoiding overlap with encapsulating layers entirely. We note that for many samples this will require virtual apertures to be defined separately for each pixel (or at least local regions of real space) instead of from diffraction patterns averaged over larger domains as was done previously^{24,36,59} and that precise automated determination of these small overlap regions is difficult for the same reason that the precise disk locations in these individual CBED patterns are hard to extract. This limitation may also be addressed by fitting regions associated with a greater number of overlapping disks to more complex expected expressions so that larger virtual apertures can be used, although such an approach requires improvements in the computational post-processing to be discussed.

V. INTENSITY FITTING TO DETERMINE INTER-LAYER STACKING

We compare multiple fitting procedures to obtain the displacements \mathbf{u} prescribed by equation 2. One approach we use involves fitting \mathbf{u}_{jk} and the coefficients A_i, B_i sequentially, such that \mathbf{u}_{jk} at each pixel location (j, k) and the coefficients for each of the twelve disks can each be fit independently and parallelized. In addition to being much faster and allowing for the coefficients to be optimized using linear least squares, we found that this use of alternating optimization⁶⁰ was also more robust to experimental noise and permitted the use of many initial guesses at each iterative step, helping to avoid local minima.

In this iterative approach, we first determine the optimal displacement vector \mathbf{u}_{jk} independently at each pixel (j, k) provided the fixed coefficients A_i, B_i . The experimental intensities are normalized, and $A_i = 0, B_i = 1$ are assumed. We used a dense uniform grid of 36 initial starting conditions to decrease the chance of obtaining local minima and constrain the values of \mathbf{u} to reside within a single unit cell such that $\mathbf{u} = c_1\mathbf{a}_1 + c_2\mathbf{a}_2$ with $|c_1| \leq 1/2, |c_2| \leq 1/2$ in terms of the separately measurable in-plane lattice vectors \mathbf{a}_1 and \mathbf{a}_2 . This results in the following over-determined equation with an easily obtainable Jacobian, which we solved using Newton non-linear least squares independently for each pixel.

$$\begin{bmatrix} I_{10} \\ \dots \\ I_{hk} \end{bmatrix} = \begin{bmatrix} A_{10} + B_{10}\cos^2(\pi c_1) \\ \dots \\ A_{hk} + B_{hk}\cos^2(\pi(hc_1 + kc_2)) \end{bmatrix} \quad (3)$$

Using these \mathbf{u}_{jk} values, we determine the optimal coefficients A_i, B_i independently for each of the twelve Bragg disk intensities I_{ijk} at each pixel (j, k) using linear least squares. Fitting the coefficients at a fixed choice of \mathbf{u} results in the following linear equation for each diffraction disk i . We note that the coefficients A_i, B_i are assumed to be independent of pixel location over the N by N pixel field of view to avoid

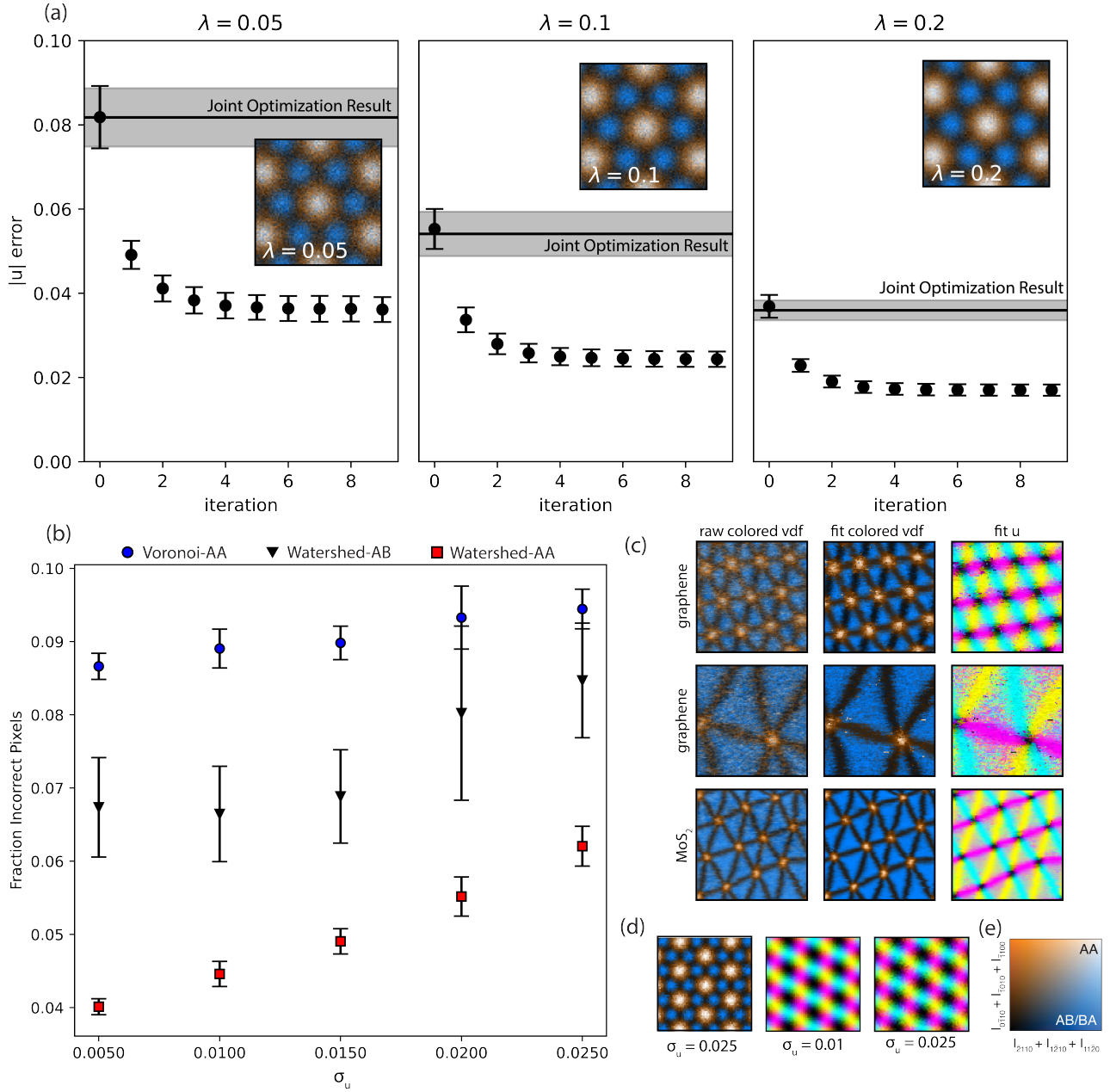


FIG. 4. **(4a)** Mean $|u|$ errors (in units of a_0) obtained through fitting intensities in the form of equation 2 (with $A=1, B=0$) using the iterative and joint optimizations described. Poisson noise is included by drawing each disk intensity independently from the Poisson distribution $P(k; \lambda I) = (\lambda I)^k \exp(-\lambda I) / k!$ where I is the noise-free intensity. A range of specified λ choices are shown, which in practice will depend on the electron dose. Noise mitigation is expected when averaging over many pixels to obtain overlap regions, increasing the effective λ . The resulting signal-to-noise ratio of the interferometry pattern is shown using a colored virtual dark field in the inset. Error bars represent the standard deviation using 25 datasets randomly generated in this manner. The result of the joint optimization is shown as a solid line and its corresponding standard deviation as the greyed region. **(4b)** The fraction of incorrectly assigned pixels using each of the three described unwrapping procedures applied to the displacement fields expected of a rigidly twisted structure (shown in 4d) with Gaussian noise of zero mean and the specified standard deviation σ_u (in units of a_0). Error bars represent the standard deviation using 25 datasets randomly generated in this manner. We note that pixels on the edge of the field of view can be incorrectly assigned even without noise in these approaches. **(4c)** Colored virtual dark fields (see Fig 4e) and displacement field maps (visualized using the color scheme defined in Fig 1c) illustrating the signal-to-noise ratios and fit efficacy of representative experimental data. **(4d)** Colored virtual dark fields and displacement field maps (visualized using the color scheme defined in Fig 1c) for artificial data assuming a rigidly twisted structure and given Gaussian noise, as used in the comparison of the unwrapping approaches in (4b). **(4e)** Color legend for virtual dark fields illustrating qualitative atomic stacking classifications.⁵⁹

over-fitting, and can be assumed to be approximately 1 and 0 respectively following normalization of I_i .

$$\underbrace{\begin{bmatrix} \cos^2(\boldsymbol{\pi}\mathbf{g}_i \cdot \mathbf{u}_{00}) & 1 \\ \cos^2(\boldsymbol{\pi}\mathbf{g}_i \cdot \mathbf{u}_{10}) & 1 \\ \dots & \dots \\ \cos^2(\boldsymbol{\pi}\mathbf{g}_i \cdot \mathbf{u}_{NN}) & 1 \end{bmatrix}}_{A_{coef}} \cdot \begin{bmatrix} A_i \\ B_i \end{bmatrix} = \underbrace{\begin{bmatrix} I_{i00} \\ I_{i10} \\ \dots \\ I_{iNN} \end{bmatrix}}_{b_{coef}} \quad (4)$$

The fitting of A_i, B_i and \mathbf{u}_{jk} are then iterated until convergence. We compare this staged optimization to a joint optimization in which the coefficients and \mathbf{u} are optimized simultaneously following one iteration of the same multi-start \mathbf{u}_{jk} optimization with fixed $A_i = 1, B_i = 0$. The mean $|\mathbf{u}|$ obtained over the full set of pixels is shown for both approaches in Fig 4a for artificial data corresponding to a rigidly twisted structure with disk intensities that exactly obey equation 2 with independent Poisson noise associated with acquisition included for each disk intensity. Representative experimental datasets are shown in Fig 4c, showing that the extent of noise included is comparable or greater than that expected of weakly scattering samples like graphene and much greater than that expected of transition metal dichalcogenides (both acquired using $\alpha = 1.7$ mrad). Fig 5a shows that the iterative approach consistently achieves a lower error in the displacements \mathbf{u} (Fig 4a). Avoidance of local extrema and noise mitigation are both active areas of research and alternative algorithms such as genetic algorithms⁶¹ could prove better than this iterative multi-start approach, but were not required for experimental data of this nature.

VI. DISPLACEMENT UNWRAPPING FOR STRAIN EXTRACTION

The displacements obtained in the fitting procedure cannot yet be differentiated to assess local strain. This is because the obtained \mathbf{u} are not uniquely determined by the data, since adding integer multiples of the lattice vectors \mathbf{a}_1 and \mathbf{a}_2 to \mathbf{u} results in the same set of intensities due to the sample's symmetry. For centro-symmetric materials, flipping the sign of \mathbf{u} also results in the same pattern. Owing to these ambiguities, the raw displacement vectors obtained are not smoothly oriented and cannot be naively differentiated, even without experimental noise or imperfections in the fitting procedure. To resolve this, we can determine the sign and lattice vector offsets needed to obtain smoothly varying displacements. While not specific to BI-obtained displacements, such a procedure is not needed when analyzing simulated data with uniform moiré domains as the effect of lattice symmetry can be accounted for by easily removing low-frequency modes. Additionally, this degeneracy does not feature in more conventional strain-mapping procedures that monitor gradual shifts in the Bragg disk locations. The problem will however generally apply when attempting to differentiate experimentally obtained displacements, given that the extent of noise is large enough that we cannot naively choose locally optimal offsets.

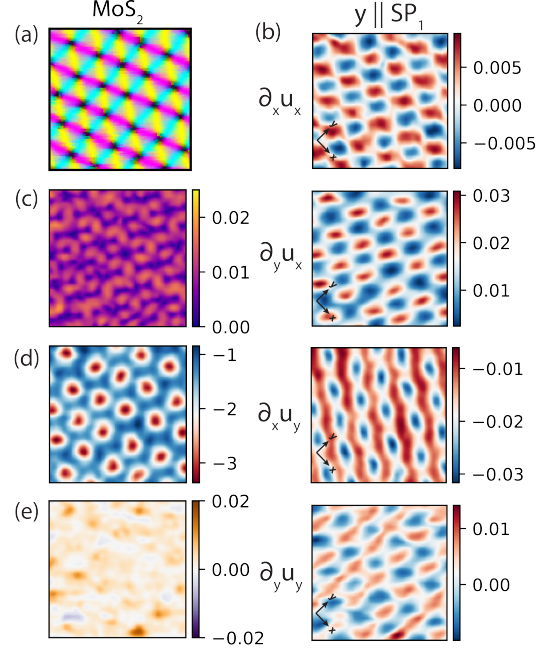


FIG. 5. **(5a)** Displacement field map (visualized using the color scheme defined in Fig 1c) for a representative experimental dataset of hBN encapsulated bilayer MoS₂ with a 1.77 degree twist, fit using the described iterative procedure. The field of view is 100 by 100 pixels, corresponding to 50 by 50 nm. **(5b)** Components of the strain tensor $\nabla \mathbf{u}_{ij}^{\text{top}}$ obtained by numerically differentiating the displacement field following unwrapping via the Watershed-AA approach. Values provided are unit-less after accounting for the difference in scale for the displacements ($a_0 = 0.315$ nm for MoS₂) and pixels (step size of 0.5 nm). Results are shown using a coordinate system where the y-axis is taken to lie along SP_1 , necessary to obtain $\nabla \cdot \mathbf{u}^{\text{top}} \approx 0$ and $\nabla \times \mathbf{u}^{\text{top}} \approx \theta_i$ in rigidly twisted structures. **(5c-e)** The corresponding engineering shear strain, local rotations $\nabla \times \mathbf{u}^{\text{top}}$ (shown in degrees), and local dilation $\nabla \cdot \mathbf{u}^{\text{top}}$

We therefore seek to find the optimal s_{jk}, n_{jk}, m_{jk} at each pixel location (j, k) given \mathbf{u}_{jk} such that the (squared) euclidean distance of $\mathbf{u}_{jk}^{\text{unwrap}}$ from all four of its neighbors is minimized, thus minimizing a quadratic cost function to variations in integer parameters.

$$\mathbf{u}_{jk}^{\text{unwrap}} = s_{jk} \mathbf{u}_{jk} + n_{jk} \mathbf{a}_1 + m_{jk} \mathbf{a}_2 \quad (5)$$

$$n_{jk}, m_{jk} \in \mathbb{Z}, s_{jk} = \pm 1 \quad (6)$$

Liberal use of integer quadratic programming is prohibitively expensive, so we considerably pre-process the data so that it need only be applied in small regions. We first pre-processed the data using physical intuition regarding its geometry, partitioning the displacements into zones of constant lattice vector offsets (n, m) , such that $n_{jk}, m_{jk} = n_i, m_i$ for all pixels (j, k) in region i .

One partitioning approach we used involves the watershed algorithm.⁶² In this method, several regions are specified (in this case the centers of the $|\mathbf{u}| \approx 0$ (AA-type) stack-

ing regions) and pixels of increasing $|\mathbf{u}|$ are successively assigned. We denote this as watershed-AA. The watershed-AA approach proved effective on the data sets with large, dispersed regions of $|\mathbf{u}| \approx 0$ stacking separated by thin boundaries, as was seen for anti-parallel aligned twisted transition metal dichalcogenides³⁶. We also investigate an alternative approach based on a Voronoi partition⁶³, where region boundaries are drawn halfway between the x_i locations. This method was successful for highly noisy data but failed when the moiré wavelength varied even marginally over the field of view.³⁶ Lastly, we investigate an approach where the watershed algorithm is applied to the angle of \mathbf{u} instead of its magnitude to select Bernal-type stacking regions for structures that minimize $|\mathbf{u}| \approx 0$ like large-angle twisted graphene and parallel aligned twisted transition metal dichalcogenides. We denote this approach as watershed-AB. After use of any of these three segmentation approaches, the values n_i, m_i are determined based on the connectivity of neighboring regions and s_{ij} is chosen to maximize a local curl. A quadratic integer program can then be applied to the pre-processed data.³⁶

We compare these three segmentation approaches on artificial $\mathbf{u}_{jk}^{\text{unwrap}}$ data corresponding to a rigidly twisted structure with Gaussian-distributed noise to model the effects of sample defects and contamination, which is then converted into u_{jk} following Eqn 4. Fig 4b shows the fraction of incorrectly assigned pixels after each segmentation approach. These results illustrate that the Watershed-AA approach performs best for the rigidly-twisted domains, but its performance declines more rapidly with increasing noise than the Voronoi approach. The Watershed-AB approach is more variable to subtle details in the applied noise, which can impact the angle of \mathbf{u} more easily than its magnitude. For applications to experimental data, the most appropriate choice will depend heavily on the morphology of the moiré pattern.

Following the unwrapping procedure, $\mathbf{u}^{\text{unwrap}}$ can then be differentiated numerically, for which we use a centered finite difference stencil. We note that the measured displacements are cell-averaged quantities, which some other stencil choices would need to account for and a factor of one half is introduced as we consider the intralayer strain $\nabla \mathbf{u}^{\text{top}}$. In practice there is often a rotation between the real-space coordinate system and that used to define \mathbf{u} , which need be accounted for.^{24,36}

Using the techniques described here, we can directly measure the moiré-scale strain in bilayer systems. Experimental strain distributions are shown in Fig 5 for MoS₂ with a twist angle of 1.77 degrees using a series of coordinate choices. The shear strain, curl, and divergence maps are shown in Fig 5c-e, expected to be uniformly 0, θ , and 0 in a rigid structure respectively. The clear local structure in 5c and 5d are consequences of atomic reconstruction, showing that MoS₂ distorts to increase the local twist angle within the $|\mathbf{u}| \approx 0$ (shown black in Fig 5a), reducing the size of these high-energy stacking regions. Simultaneously, the distortion decreases the local twist angle within the low-energy stacking regions (Fig 5d). These two rotational effects act in a manner that accumulates shear strain along their boundaries (Fig 5c) while the dilational strain associated with uniform stretching of the lat-

tice remains negligible (Fig 5e).³⁶

VII. CONCLUSION

We have outlined and analyzed various numerical and instrumental limitations for the BI technique and presented solutions to generalize its applicability to a wider range of bilayer systems. Future work will aim to expand this method for use in the limit of smaller converged probe sizes and more general samples. This may involve any of the discussed strategies including the use of more precisely defined non-spherical virtual apertures to enable smaller CBED probes, fitting disk locations in tandem with their intensities, more involved post-processing techniques along the lines of those discussed for interpreting multi-layer overlap regions, and improvements to the algorithms used.

ACKNOWLEDGMENTS

This material is based upon work supported by the US National Science Foundation Early Career Development Program (CAREER), under award no. 2238196 (D.K.B). I.M.C. acknowledges a pre-doctoral fellowship award under contract FA9550-21-F-0003 through the National Defense Science and Engineering Graduate (NDSEG) Fellowship Program, sponsored by the Air Force Research Laboratory (AFRL), the Office of Naval Research (ONR) and the Army Research Office (ARO). Work at the Molecular Foundry was supported by the Office of Science, Office of Basic Energy Sciences, of the U.S. Department of Energy under Contract No. DE-AC02-05CH11231.

CONFLICT OF INTEREST

The authors have no conflicts to disclose.

DATA AVAILABILITY STATEMENT

The data that support the findings of this study are available within the article.

¹D. Huang, J. Choi, C.-K. Shih, and X. Li, “Excitons in semiconductor moiré superlattices,” *Nat. Nanotechnol.* **17**, 227–238 (2022).

²K. F. Mak and J. Shan, “Semiconductor moiré materials,” *Nat. Nanotechnol.* **17**, 686–696 (2022).

³N. Zhang, A. Surrente, M. Baranowski, D. K. Maude, P. Gant, A. Castellanos-Gomez, and P. Plochocka, “Moiré intralayer excitons in a MoSe₂/MoS₂ heterostructure,” *Nano Lett.* **18**, 7651–7657 (2018).

⁴K. L. Seyler, P. Rivera, H. Yu, N. P. Wilson, E. L. Ray, D. G. Mandrus, J. Yan, W. Yao, and X. Xu, “Signatures of moiré-trapped valley excitons in MoSe₂/WSe₂ heterobilayers,” *Nature* **567**, 66–70 (2019).

⁵E. M. Alexeev, D. A. Ruiz-Tijerina, M. Danovich, M. J. Hamer, D. J. Terry, P. K. Nayak, S. Ahn, S. Pak, J. Lee, J. I. Sohn, *et al.*, “Resonantly hybridized excitons in moiré superlattices in van der waals heterostructures,” *Nature* **567**, 81–86 (2019).

- ⁶C. Jin, E. C. Regan, A. Yan, M. Iqbal Bakti Utama, D. Wang, S. Zhao, Y. Qin, S. Yang, Z. Zheng, S. Shi, *et al.*, “Observation of moiré excitons in WSe₂/WS₂ heterostructure superlattices,” *Nature* **567**, 76–80 (2019).
- ⁷K. Tran, G. Moody, F. Wu, X. Lu, J. Choi, K. Kim, A. Rai, D. A. Sanchez, J. Qian, A. Singh, *et al.*, “Evidence for moiré excitons in van der waals heterostructures,” *Nature* **567**, 71–75 (2019).
- ⁸E. Liu, E. Barré, J. van Baren, M. Wilson, T. Taniguchi, K. Watanabe, Y.-T. Cui, N. M. Gabor, T. F. Heinz, Y.-C. Chang, *et al.*, “Signatures of moiré trions in WSe₂/MoSe₂ heterobilayers,” *Nature* **594**, 46–50 (2021).
- ⁹M. Dandu, G. Gupta, P. Dasika, K. Watanabe, T. Taniguchi, and K. Majumdar, “Electrically tunable localized versus delocalized intralayer moiré excitons and trions in a twisted MoS₂ bilayer,” *ACS Nano* **16**, 8983–8992 (2022).
- ¹⁰M. H. Naik, E. C. Regan, Z. Zhang, Y.-H. Chan, Z. Li, D. Wang, Y. Yoon, C. S. Ong, W. Zhao, S. Zhao, *et al.*, “Intralayer charge-transfer moiré excitons in van der waals superlattices,” *Nature* **609**, 52–57 (2022).
- ¹¹S. Susarla, M. H. Naik, D. D. Blach, J. Zipfel, T. Taniguchi, K. Watanabe, L. Huang, R. Ramesh, F. H. da Jornada, S. G. Louie, *et al.*, “Hyperspectral imaging of excitons within a moiré unit-cell with a sub-nanometer electron probe,” Preprint at arXiv:2207.13823 (2022).
- ¹²L. Balents, C. R. Dean, D. K. Efetov, and A. F. Young, “Superconductivity and strong correlations in moiré flat bands,” *Nat. Phys.* **16**, 725–733 (2020).
- ¹³C. N. Lau, M. W. Bockrath, K. F. Mak, and F. Zhang, “Reproducibility in the fabrication and physics of moiré materials,” *Nature* **602**, 41–50 (2022).
- ¹⁴Y. Tang, L. Li, T. Li, Y. Xu, S. Liu, K. Barmak, K. Watanabe, T. Taniguchi, A. H. MacDonald, J. Shan, *et al.*, “Simulation of hubbard model physics in WSe₂/WS₂ moiré superlattices,” *Nature* **579**, 353–358 (2020).
- ¹⁵L. Wang, E.-M. Shih, A. Ghiotto, L. Xian, D. A. Rhodes, C. Tan, M. Claassen, D. M. Kennes, Y. Bai, B. Kim, *et al.*, “Correlated electronic phases in twisted bilayer transition metal dichalcogenides,” *Nat. Mater.* **19**, 861–866 (2020).
- ¹⁶E. C. Regan, D. Wang, C. Jin, M. I. Bakti Utama, B. Gao, X. Wei, S. Zhao, W. Zhao, Z. Zhang, K. Yumigeta, *et al.*, “Mott and generalized wigner crystal states in WSe₂/WS₂ moiré superlattices,” *Nature* **579**, 359–363 (2020).
- ¹⁷Y. Xu, S. Liu, D. A. Rhodes, K. Watanabe, T. Taniguchi, J. Hone, V. Elser, K. F. Mak, and J. Shan, “Correlated insulating states at fractional fillings of moiré superlattices,” *Nature* **587**, 214–218 (2020).
- ¹⁸H. Li, S. Li, E. C. Regan, D. Wang, W. Zhao, S. Kahn, K. Yumigeta, M. Blei, T. Taniguchi, K. Watanabe, *et al.*, “Imaging two-dimensional generalized wigner crystals,” *Nature* **597**, 650–654 (2021).
- ¹⁹X. Huang, T. Wang, S. Miao, C. Wang, Z. Li, Z. Lian, T. Taniguchi, K. Watanabe, S. Okamoto, D. Xiao, *et al.*, “Correlated insulating states at fractional fillings of the WS₂/WSe₂ moiré lattice,” *Nat. Phys.* **17**, 715–719 (2021).
- ²⁰Y. Xu, K. Kang, K. Watanabe, T. Taniguchi, K. F. Mak, and J. Shan, “A tunable bilayer hubbard model in twisted WSe₂,” *Nat. Nanotechnol.* **17**, 934–939 (2022).
- ²¹H. Yoo, R. Engelke, S. Carr, S. Fang, K. Zhang, P. Cazeaux, S. H. Sung, R. Hovden, A. W. Tsun, T. Taniguchi, *et al.*, “Atomic and electronic reconstruction at the van der waals interface in twisted bilayer graphene,” *Nat. Mater.* **18**, 448–453 (2019).
- ²²A. Weston, Y. Zou, V. Enaldiev, A. Summerfield, N. Clark, V. Zólyomi, A. Graham, C. Yelgel, S. Magorrian, M. Zhou, *et al.*, “Atomic reconstruction in twisted bilayers of transition metal dichalcogenides,” *Nat. Nanotechnol.* **15**, 592–597 (2020).
- ²³M. R. Rosenberger, H.-J. Chuang, M. Phillips, V. P. Oleshko, K. M. McCreary, S. V. Sivaram, C. S. Hellberg, and B. T. Jonker, “Twist angle-dependent atomic reconstruction and moiré patterns in transition metal dichalcogenide heterostructures,” *ACS Nano* **14**, 4550–4558 (2020).
- ²⁴N. P. Kazmierczak, M. Van Winkle, C. Ophus, K. C. Bustillo, S. Carr, H. G. Brown, J. Ciston, T. Taniguchi, K. Watanabe, and D. K. Bediako, “Strain fields in twisted bilayer graphene,” *Nat. Mater.* **20**, 956–963 (2021).
- ²⁵H. Li, S. Li, M. H. Naik, J. Xie, X. Li, J. Wang, E. Regan, D. Wang, W. Zhao, S. Zhao, *et al.*, “Imaging moiré flat bands in three-dimensional reconstructed WSe₂/WS₂ superlattices,” *Nat. Mater.* **20**, 945–950 (2021).
- ²⁶S. H. Sung, Y. M. Goh, H. Yoo, R. Engelke, H. Xie, K. Zhang, Z. Li, A. Ye, P. B. Deotare, E. B. Tadmor, *et al.*, “Torsional periodic lattice distortions and diffraction of twisted 2d materials,” arXiv preprint arXiv:2203.06510 (2022).
- ²⁷S. Shabani, D. Halbertal, W. Wu, M. Chen, S. Liu, J. Hone, W. Yao, D. N. Basov, X. Zhu, and A. N. Pasupathy, “Deep moiré potentials in twisted transition metal dichalcogenide bilayers,” *Nat. Phys.* **17**, 720–725 (2021).
- ²⁸M. H. Naik, S. Kundu, I. Maity, and M. Jain, “Origin and evolution of ultra-flat bands in twisted bilayer transition metal dichalcogenides: Realization of triangular quantum dots,” *Phys. Rev. B* **102**, 075413 (2020).
- ²⁹E. Li, J.-X. Hu, X. Feng, Z. Zhou, L. An, K. T. Law, N. Wang, and N. Lin, “Lattice reconstruction induced multiple ultra-flat bands in twisted bilayer WSe₂,” *Nat. Commun.* **12**, 1–7 (2021).
- ³⁰M. H. Naik and M. Jain, “Ultraflatbands and shear solitons in moiré patterns of twisted bilayer transition metal dichalcogenides,” *Phys. Rev. Lett.* **121**, 266401 (2018).
- ³¹V. Enaldiev, V. Zólyomi, C. Yelgel, S. Magorrian, and V. Fal’ko, “Stacking domains and dislocation networks in marginally twisted bilayers of transition metal dichalcogenides,” *Phys. Rev. Lett.* **124**, 206101 (2020).
- ³²F. Ferreira, S. Magorrian, V. Enaldiev, D. Ruiz-Tijerina, and V. Fal’ko, “Band energy landscapes in twisted homobilayers of transition metal dichalcogenides,” *Appl. Phys. Lett.* **118**, 241602 (2021).
- ³³C. Ophus, P. Ercius, M. Sarahan, C. Czarnik, and J. Ciston, “Recording and using 4d-stem datasets in materials science,” *Microscopy and Microanalysis* **20**, 62–63 (2014).
- ³⁴T. Latychevskaia, C. R. Woods, Y. B. Wang, M. Holwill, E. Prestat, S. J. Haigh, and K. S. Novoselov, “Convergent beam electron holography for analysis of van der waals heterostructures,” *Proceedings of the National Academy of Sciences* **115**, 7473–7478 (2018).
- ³⁵C. Ophus, “Four-dimensional scanning transmission electron microscopy (4d-stem): From scanning nanodiffraction to ptychography and beyond,” *Microsc. Microanal.* **25**, 563–582 (2019).
- ³⁶M. Van Winkle, I. M. Craig, S. Carr, M. Dandu, K. C. Bustillo, J. Ciston, C. Ophus, T. Taniguchi, K. Watanabe, A. Raja, *et al.*, “Rotational and dilational reconstruction in transition metal dichalcogenide moiré bilayers,” *Nature communications* **14**, 2989 (2023).
- ³⁷M. J. Zachman, J. Madsen, X. Zhang, P. M. Ajayan, T. Susi, and M. Chi, “Interferometric 4d-stem for lattice distortion and interlayer spacing measurements of bilayer and trilayer 2d materials,” *Small* **17**, 2100388 (2021).
- ³⁸D. Mukherjee, J. T. Gamler, S. E. Skrabalak, and R. R. Unocic, “Lattice strain measurement of core@ shell electrocatalysts with 4d scanning transmission electron microscopy nanobeam electron diffraction,” *ACS Catalysis* **10**, 5529–5541 (2020).
- ³⁹R. Yuan, J. Zhang, and J.-M. Zuo, “Lattice strain mapping using circular hough transform for electron diffraction disk detection,” *Ultramicroscopy* **207**, 112837 (2019).
- ⁴⁰J. Munshi, A. Rakowski, B. H. Savitzky, S. E. Zeltmann, J. Ciston, M. Henderson, S. Cholia, A. M. Minor, M. K. Chan, and C. Ophus, “Disentangling multiple scattering with deep learning: application to strain mapping from electron diffraction patterns,” *npj Computational Materials* **8**, 254 (2022).
- ⁴¹B. Sari, S. E. Zeltmann, C. Zhao, P. M. Pelz, A. Javey, A. M. Minor, C. Ophus, and M. C. Scott, “Analysis of strain and defects in tellurium-wse₂ moiré heterostructures using scanning nanodiffraction,” *ACS nano* **17**, 22326–22333 (2023).
- ⁴²C. Mahr, K. Müller-Caspary, T. Grieb, F. F. Krause, M. Schowalter, and A. Rosenauer, “Accurate measurement of strain at interfaces in 4d-stem: A comparison of various methods,” *Ultramicroscopy* **221**, 113196 (2021).
- ⁴³C. Shi, N. Mao, K. Zhang, T. Zhang, M.-H. Chiu, K. Ashen, B. Wang, X. Tang, G. Guo, S. Lei, *et al.*, “Domain-dependent strain and stacking in two-dimensional van der waals ferroelectrics,” *Nature communications* **14**, 7168 (2023).
- ⁴⁴S. E. Zeltmann, A. Müller, K. C. Bustillo, B. Savitzky, L. Hughes, A. M. Minor, and C. Ophus, “Patterned probes for high precision 4d-stem bragg measurements,” *Ultramicroscopy* **209**, 112890 (2020).
- ⁴⁵Y. Jiang, Z. Chen, Y. Han, P. Deb, H. Gao, S. Xie, P. Purohit, M. W. Tate, J. Park, S. M. Gruner, *et al.*, “Electron ptychography of 2d materials to deep sub-ångström resolution,” *Nature* **559**, 343–349 (2018).
- ⁴⁶Z. Chen, M. Odstrcil, Y. Jiang, Y. Han, M.-H. Chiu, L.-J. Li, and D. A. Muller, “Mixed-state electron ptychography enables sub-ångström resolution imaging with picometer precision at low dose,” *Nature communications* **11**, 2994 (2020).
- ⁴⁷W. Yang, H. Sha, J. Cui, L. Mao, and R. Yu, “Local-orbital ptychography for ultrahigh-resolution imaging,” *Nature Nanotechnology*, 1–6 (2024).

- ⁴⁸P. M. Pelz, W. X. Qiu, R. Bücker, G. Kassier, and R. D. Miller, “Low-dose cryo electron ptychography via non-convex bayesian optimization,” *Scientific reports* **7**, 9883 (2017).
- ⁴⁹W. S. Slaughter, “Kinematics,” in *The Linearized Theory of Elasticity* (Birkhäuser, Boston, MA, 2002) pp. 97–155.
- ⁵⁰J. Madsen and T. Susi, “The abtem code: transmission electron microscopy from first principles,” *Open Research Europe* **1** (2021).
- ⁵¹J. M. Cowley and A. F. Moodie, “The scattering of electrons by atoms and crystals. i. a new theoretical approach,” *Acta Crystallographica* **10**, 609–619 (1957).
- ⁵²O. Scherzer, “The theoretical resolution limit of the electron microscope,” *Journal of Applied Physics* **20**, 20–29 (1949).
- ⁵³E. J. Kirkland, *Advanced computing in electron microscopy*, Vol. 12 (Springer, 1998).
- ⁵⁴M. Weyland and D. A. Muller, “Tuning the convergence angle for optimum stem performance,” arXiv preprint arXiv:2008.12870 (2020).
- ⁵⁵S. Kretschmer, T. Lehnert, U. Kaiser, and A. V. Krashennikov, “Formation of defects in two-dimensional mos2 in the transmission electron microscope at electron energies below the knock-on threshold: the role of electronic excitations,” *Nano letters* **20**, 2865–2870 (2020).
- ⁵⁶D. C. Bell, M. Mankin, R. W. Day, and N. Erdman, “Successful application of low voltage electron microscopy to practical materials problems,” *Ultramicroscopy* **145**, 56–65 (2014).
- ⁵⁷R. Egerton, “Mechanisms of radiation damage in beam-sensitive specimens, for tem accelerating voltages between 10 and 300 kv,” *Microscopy research and technique* **75**, 1550–1556 (2012).
- ⁵⁸E. James and N. Browning, “Practical aspects of atomic resolution imaging and analysis in stem,” *Ultramicroscopy* **78**, 125–139 (1999).
- ⁵⁹I. M. Craig, M. Van Winkle, C. Groschner, K. Zhang, N. Dowlatshahi, Z. Zhu, T. Taniguchi, K. Watanabe, S. M. Griffin, and D. K. Bediako, “Local atomic stacking and symmetry in twisted graphene trilayers,” *Nature Materials* , 1–8 (2024).
- ⁶⁰J. C. Bezdek and R. J. Hathaway, “Convergence of alternating optimization,” *Neural, Parallel & Scientific Computations* **11**, 351–368 (2003).
- ⁶¹S. Mirjalili and S. Mirjalili, “Genetic algorithm,” *Evolutionary algorithms and neural networks: Theory and applications* , 43–55 (2019).
- ⁶²A. S. Kornilov and I. V. Safonov, “An overview of watershed algorithm implementations in open source libraries,” *Journal of Imaging* **4**, 123 (2018).
- ⁶³A. Okabe, B. Boots, K. Sugihara, and S. N. Chiu, “Spatial tessellations: concepts and applications of voronoi diagrams,” (2009).